

LITHOLOGICAL MAPPING AND IDENTIFICATION OF ARGILLIC AND PROPYLITIC ALTERATION ZONES AT ANJERD VOLCANIC TERRAIN**MAPEAMENTO LITOLÓGICO E IDENTIFICAÇÃO DE ZONAS DE ALTERAÇÃO ARGÍLICA E PROPILÍTICA NO TERRENO VULCÂNICO DE ANJERD**Majid Bagheri¹Afshin Ashja-Ardalan*²Alireza Gangi³Saeid Hakimi Asiabar⁴Mohammad Ali Arian⁵**ABSTRACT**

Anjerd area is part of Arasbaran volcanic-magmatic terrain in northwestern Iran. The area is covered by multiple intrusive bodies of diverse compositions, volcanic, volcanoclastic, sedimentary and young alluvial deposits. The usefulness of Advanced Spaceborne Thermal Emission and Reflection Radiometer (ASTER) data for the lithologic mapping of the area and identification of alteration zones is investigated in this study. To carry out the study, one ASTER frame was atmospherically calibrated by Internal Average Relative Reflectance (IARR). The False Color Composite (FCC) and Principal Component Analysis (PCA) images were used for discriminating lithologic units along with Spectral Angle Mapper (SAM) and Matched Filtering (MF). The pure endmember image spectra were extracted from Pixel Purity (PPI) algorithm. The results showed that PCA and FCC can be used to discriminate sedimentary rocks from magmatic and volcanic rocks. Because feldspars and quartz are relatively featureless in shortwave infrared (SWIR) spectral region the methods were not capable to distinguish between various magmatic rocks except for basalts with darker color and higher pyroxene content. The MF gave better results than SAM algorithm and therefore MF is recommended over SAM for studying similar terrains. The argillic and propylitic alteration zones were detected by band ratios. The results showed that MF algorithm in combination with band ratios can be used to distinguish magmatic rocks from sedimentary rocks and delineate the alteration zones.

KEYWORDS: LITHOLOGICAL MAPPING; ARGILLIC; PROPYLITIC; ALTERATION ZONES; ANJERD VOLCANIC TERRAIN.

¹PhD Candidate, Department of Geology, North Tehran Branch, Islamic Azad University, Tehran, Iran.

m_bagheri@iau-tnb.ac.ir ORCID: <https://orcid.org/0000-0001-7394-262X>

²Assistant Professor, Department of Geology, North Tehran Branch, Islamic Azad University, Tehran, Iran.

*Corresponding author. a_ashjaardalan@iau-tnb.ac.ir ORCID: <https://orcid.org/0000-0002-1800-9594>

³ Assistant Professor, Department of Geology, Lahijan Branch, Islamic Azad University, Gilan, Iran.

arganji@liau.ac.ir ORCID: <http://orcid.org/0000-0002-8670-6869>

⁴Assistant Professor, Department of Geology, Lahijan Branch, Islamic Azad University, Gilan, Iran.

saeid.h.asiabar@gmail.com ORCID: <https://orcid.org/0000-0003-3120-4498>

⁵ Assistant Professor, Department of Geology, North Tehran Branch, Islamic Azad University, Tehran, Iran.

m_arian@iau-tnb.ac.ir ORCID: <https://orcid.org/0000-0002-7877-0684>

RESUMO

A área de Anjerd faz parte do terreno magmático-vulcânico de Arasbaran, no noroeste do Irã. A área é recoberta por múltiplos corpos intrusivos de diversas composições, depósitos vulcânicos, vulcanoclásticos, sedimentares e jovens aluviais. A utilidade dos dados do Radiômetro de Emissão Térmica e Reflexão Espacial Avançado (ASTER) para o mapeamento litológico da área e identificação de zonas de alteração é o tema deste estudo. Para a condução da pesquisa, um quadro ASTER foi calibrado de forma atmosférica por meio de refletância relativa média interna (IARR). A análise das imagens foram realizadas por Composição Falsa Cor (FCC) e Análise de Componentes Principais (PCA) que permitiram discriminar unidades litológicas juntamente com Spectral Angle Mapper (SAM) e Matched Filtering (MF). Os espectros de imagem de membro final puro foram extraídos do algoritmo Pixel Purity (PPI). Os resultados mostraram que o PCA e o FCC podem ser usados para discriminar rochas sedimentares de rochas magmáticas e vulcânicas. Como os feldspatos e o quartzo são relativamente sem características na região espectral do infravermelho de ondas curtas (SWIR), os métodos não foram capazes de distinguir entre várias rochas magmáticas, exceto para basaltos com cor mais escura e maior conteúdo de piroxênio. O MF deu melhores resultados do que o algoritmo SAM e, portanto, o MF é recomendado em vez do SAM para estudar terrenos semelhantes. As zonas de alteração argílica e propilítica foram detectadas por razões de bandas. Os resultados mostraram que o algoritmo MF em combinação com razões de bandas pode ser usado para distinguir rochas magmáticas de rochas sedimentares e delinear as zonas de alteração.

PALAVRAS-CHAVE: MAPEAMENTO LITOLÓGICO; ARGÍLICO; PROPILÍTICO; ZONAS DE ALTERAÇÃO; TERRENO VULCÂNICO DE ANJERD.

INTRODUCTION

Advanced Spaceborne Thermal Emission and Reflection Radiometer (ASTER) on board the Earth Observing System (EOS) Terra satellite was launched in 2000 and provides tools for land cover mapping. The ASTER sensor acquires multispectral data in 14 bands of which 5 bands are located in the the mid-infrared, or thermal (8–14 μm) region of the electromagnetic spectrum. The other 9 bands are located in the SWIR (1.4 to 2.5 μm) spectral region are mainly used to detect carbonate, and clay minerals (Rockwell, Hofstra, 2008). The Anjerd area is part of the Arasbaran zone in Iran and is mainly composed of volcanic and magmatic rocks which have introduced into sedimentary rocks. Due to effervescence of magmatic effluents the area has been mineralized at some localities. ASTER images have not been previously extensively used to map magmatic terrains because spectral features of minerals in igneous rocks are similar to each other. In this study we have tried mapping the study area by ASTER imagery utilizing a combination of methods such as pixel purity index,

spectral angle mapper, and various band ratios. The output of various mapping methods are compared to each other. In addition to main lithologic units the alteration zones of argillic and propylitic alteration are also mapped. The resultant lithologic map produced by ASTER imagery was assessed by overlying it on the available geologic maps of the study area by sampling of rock samples.

GEOLOGY

The study area is located 25 to 70 km to the northwest of Ahar town in Eastern Azarbaijan province, Iran. The study area has a coverage about 170 square kilometers and is a part of the Arasbaran region and Alborz magmatic zone (Alavi, 2007; Yazdi *et. al.*, 2017, Baratian *et. al.*, 2020; Yazdi *et. al.*, 2019, 2019a; Jamshidibadr, *et. al.*, 2020) with rugged terrain. The granites, monzogranites, and other types of igneous and volcanic rocks cover about 50% of the region. During Late Eocene to Oligocene, multiple phases of igneous and volcanic activity have led to the formation of abundant intrusions, volcanic rocks, and tuff in the region (Agard *et. al.*, 2011). The magmatism has led to contact metamorphism, metasomatism, and formation of copper porphyry deposits, and metamorphic rocks such as hornfels (Bazin, Hübner, 1969; Hezarkhani, 2006; Agard *et. al.*, 2011; Ashrafi *et. al.*, 2018).

The sedimentary rocks in the study area mostly belong to Cretaceous which are more abundant at the north and southern part of the study area. The highest peak in the study area with an elevation of 2640m belongs to Siur Daghy intrusive body which intruded Cretaceous sedimentary and volcanic rocks. Skarn bodies, silicification, recrystallization, and hornfels are observed at the contact with the intrusion (Mollai, 1991; Mollai *et. al.*, 2009; Mollai *et. al.*, 2009a, Nazemi *et. al.*, 2019; Ghadimi, Khavari, 2019; Yasrebi, Hezarkhani, 2019). At the southern part of the area the terrain is relatively flat and Neogene sedimentary and alluvial deposits are abundant. A brief description of the lithologic description of rock units in the study area is given below.

The rock units observed in the study area include sedimentary rocks, volcanoclastic rocks, volcanic and igneous rocks. In the geologic map of the area the sedimentary rocks are

denoted by symbols such as Kl1 , Kl,sh, Ksh, Ks,sh depending on the proportion of sedimentary and volcanoclastic constituents.

Kl1 is mainly composed of limestone, whereas Kl,sh, Ksh, Ks, and Ks,sh are composed of shale, sandstone, and minor limestone. The Ksh sedimentary unit is partially transformed to hornfels and sericitized schists due to slight metamorphism. Many sedimentary rock units are not pure sedimentary rocks, but compose a significant amount of volcanoclastic materials and tuff. Conglomerates and consolidated alluvial deposits such as Ksh,t , PIQc, Qt1, and PIQc have significant amounts of volcanoclastic material and andesitic tuff in addition to limestone and sandstone. Alluvium deposits such as Qt2, Qf, Qsc, Qdf, Qds, Qc, Qal all constitute a variety of clastic materials derived from older sedimentary and volcanic rocks. In the study area, lithologic units are rarely distinguished into age groups. However, a brief description of lithologic units is provided below.

Ksh,t is of Cretaceous age and is composed of shale, agglomerate, tuff, and intermediate volcanic rocks such as andesite and dacite. The contact metamorphism related to the Shiur Daghy intrusion has led to formation of hornfels at Ksh,t unit. Ktc is composed of trachyandesite, and latite, and is affected by epidotitization. Kan is composed of andesitic basalt and basalt whose plagioclase minerals are altered to clay minerals, chlorite, carbonate minerals, and iron oxides. Kda, and Ev are composed of dacite, trachyandesite, latite, and andesite. Kvr, is composed of Rhyolite, dacite, and acidic tuff whose feldspars and ferromagnesian minerals are converted to sericite and iron oxides. Qtb, Qan, and Qb are composed of dark basalt and trachybasalt with phenocrysts of plagioclase, and pyroxene. Emp is composed of latite with intense sericitization. Kst, Kv, and Kt,sh, are composed of intercalations of tuff, shale and sandstone. Eag is composed of andesitic volcanic rocks, and agglomerates with intense alteration. Plla is a lahar deposit composed of andesite and dacite with siliceous fragments.

Intrusive bodies in the area include quartz monzonite, and quartz-monzodiorite of Shiur Daghy intrusion (qzmz-mzd). The intrusion shows fractionation of ferromagnesian

minerals and inhomogeneity from one locality to another. The intrusion has been oxidative and contains magmatic magnetite. Ferromagnesian minerals include amphibole and biotite. Some epidote, chlorite, and sericite are observed as a consequence of alteration. A small copper deposit is formed at the contact of the intrusion and mostly limestones units at the northern contact of with intrusion (Anjerd skarn deposit) (Hezarkhani, 2007; Tarabi *et al.*, 2019). Other intrusive bodies in the area are of quartz monzodiorite (d-qmd), granite (g), granodiorite (md-gb), and syenogabbro (sn-gb) composition (Mollai *et al.*, 2009a).

The hornfels rock unit (hp) at the contact with Shiur Daghy intrusion is composed of biotite, andalusite, cordierite, feldspar, and sillimanite (Babakhani *et al.*, 1990). Overall, in metabasites, metamorphism at the contact with intrusions has led to formation of epidote, actinolite, hornblende, and clinopyroxene is abundant, whilst in calc-silicate rocks, epidote, tremolite, alkali feldspar, phlogopite, garnet, clinopyroxene are more abundant. The skarn (sk) at the contact with Shiur Daghy intrusion is composed of garnet, pyroxene, actinolite, scapolite, and epidote with minor sulfide and oxide minerals, in addition to carbonate minerals which are very abundant. The hal rock unit is composed of epidote, albite, actinolite, calcite, quartz, chlorite, and garnet. The rock is black in color. The relict of original minerals is observed as plagioclase altered to clay minerals and amphibole. The traces of copper mineralization are observed as malachite (Hezarkhani, 2007).

The simplified lithological map of the study area is shown in figure 1.

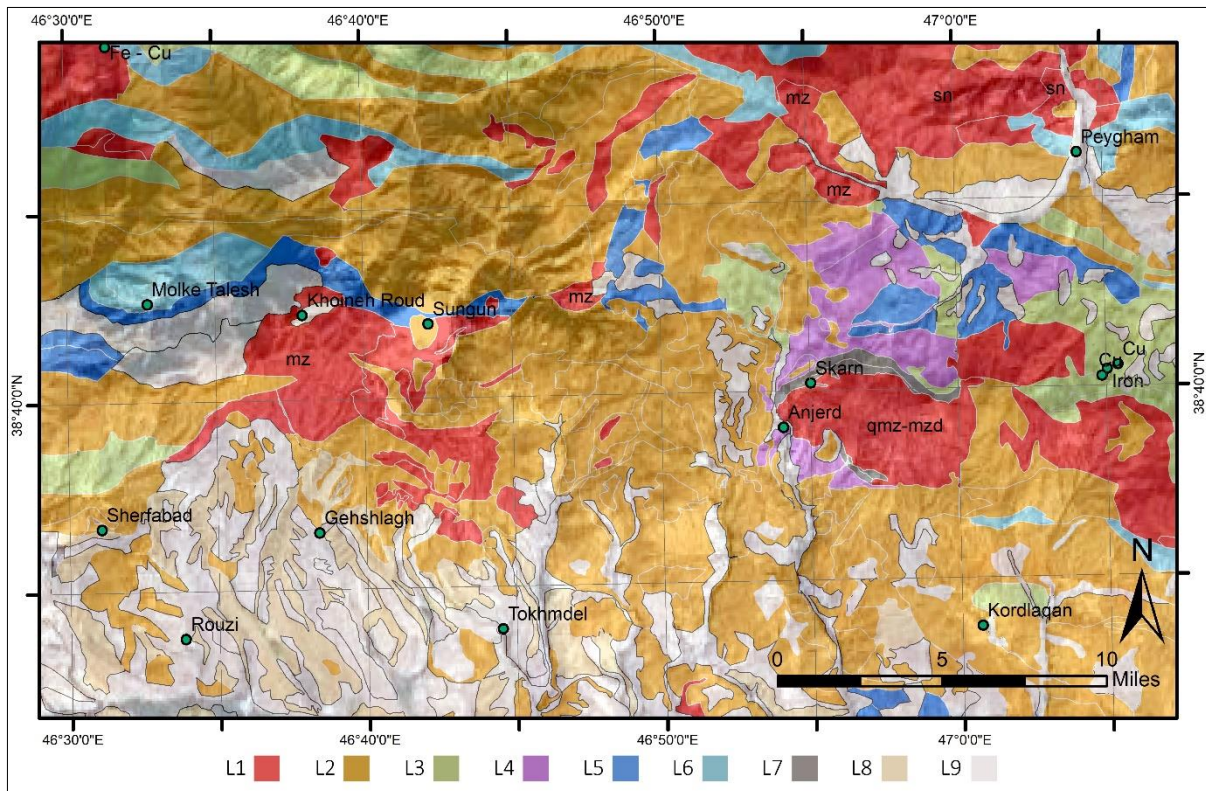


Figure 1. The lithologic map of the study area. L1: igneous rocks and magmatic intrusions, L2: volcanic rocks, L3: tuff and volcanics, L4: shale, L5: sandstones, L6: limestone, L7: metamorphic rocks, L8: conglomerate, L9: alluvium.

Source: Authors (2021).

METHODS

ATMOSPHERIC CORRECTION AND IMAGE PROCESSING

For image processing purposes, three VNIR spectral bands and six SWIR spectral bands of ASTER were stacked upon each other and then resampled to 15m spatial resolution of ASTER bands 1 to 3.

Satellite images are often corrected for atmospheric effects before being used as inputs to spectral detection algorithms (Bernstein *et. al.* 2012, Richter and Schläpfer 2012). The method used for atmospheric correction of the image was Internal Average Relative Reflectance (IARR) introduced by Fred A. Kruse (1988). IARR is a method (Fred A. Kruse, 1988) that does not need any data about the conditions of the atmosphere and uses data derived from the image bands themselves. IARR works can be used sparsely vegetated regions and when atmospheric data needed for rigorous atmospheric correction by radiative transfer

codes are unavailable (RSI, 2004; Gao *et. al.*, 2009). This method has already been used with success in several studies in arid and semiarid regions (Kruse, 1988; Ben-Dor, Kruse, 1994; Rasouli, Beirami, Tangestani, 2020). In IARR calibration, the radiance of each pixel is normalized to the average radiance of the spectral band. (Kruse, 1988). The reflectance values obtained by IARR are relative reflectance and the values cannot be directly compared with the laboratory spectra of materials. However, the IARR image would give the shape of the absorption features (Kruse, 1988).

PRINCIPAL COMPONENT ANALYSIS

The principal component analysis (PCA) is a statistical method for transforming remote sensing data into a new orthogonal space where dimensionality of the data are reduced (Yamaguchi, Naito, 2003; Rajendran *et. al.*, 2011; Asadzadeh, Souza Filho, 2016). Hence, the most prominent differences in the spectral features of the image pixels can be easily observed on PCA images. PCA works by calculating the correlation coefficient between the pixels and rotating the principal space vectors so that the principal vectors coincide with the direction of most variability in the data (Crosta, McMoore, 1989). A false color composite of the PCA bands is most often used to distinguish lithologies from each other (Tangestani *et. al.*, 2008; Rajendran *et. al.*, 2011).

EXTRACTION OF PURE SPECTRA

The shapes of the ASTER image spectra are different from the laboratory spectra due to presence of variable spectral material mixtures, mineral grain size variations (Zaini *et. al.*, 2012) and residual atmospheric absorption features (Richter, Schläpfer, 2012). Therefore, the laboratory spectra cannot be used as a reference image classification and detection of target materials, even if the spectra are resampled to ASTER band passes. Therefore, in order to increase the efficacy of mapping algorithms, it is important to select the most pure spectra from the image (Boardman *et. al.*, 1995). One of the most efficient methods to extract pure spectra from the image is pixel purity index (PPI) procedure (Boardman *et. al.*, 1995). The pixel purity index algorithm projects pixel spectra onto a randomly selected vector in the

space and then counts the number of times that each pixel is projected at the extreme ends of the random vector. The pixels with the highest number of times projected at the extreme ends of the random vectors are selected as pixels with purest spectrum. To decrease the effect of noise on pixel projection, pixel purity index procedure uses noise normalized transformed (MNF) images (Rowan, Mars, 2003; RSI, 2004). MNF images are similar to PCA images except for the fact that image is transformed by choosing principal space vectors in such a way that signal to noise ratio is highest (Rajendran *et. al.*, 2013).

BAND RATIOS AND IMAGE ENHANCEMENT

ASTER ratio images have been used successfully and extensively to depict spectral compositional variations by eliminating albedo effects related to topographic slope variations, illumination conditions, and grain size variations (Rowan and Mars 2003, Rowan *et. al.* 2005). Band ratios are so sensitive to spectral variations that they can even be used to distinguish dolomite from calcite (Beirami, Tangestani, 2020). Because band ratios are insensitive to illumination conditions, they can be easily used for lithological mapping in an image calibrated by IAR procedure (Kruse, 1988; Rowan *et. al.*, 2005; Crowley *et. al.*, 1989, Crowley, 1993; Rowan, Mars, 2003; Rowan *et. al.*, 2005; Beirami, Tangestani, 2020) in this study.

SPECTRAL ANGLE MAPPER

Spectral Angle Mapper algorithm (SAM) provides a measure of similarity between reference and unknown spectra by computing the angle between the two spectra assuming that the two spectra are the vector values in an n-dimensional space (Kruse *et. al.*, 1993). The result of SAM is an image that shows the spectral angle between the reference spectra and the image pixel spectra. Pixels with lower divergence angles or in other words darker pixels match reference spectra more closely. SAM is insensitive to scene illumination conditions (Kruse *et. al.*, 1993) and therefore can be used on IAR images.

MATCHED FILTERING

Matched Filtering (MF) is a spectral unmixing method that finds abundances of defined spectral endmembers using a partial unmixing procedure. The MF method was originally developed by Boardman *et. al.* (1995). The main advantage of MF is that it is not necessary to know all image endmembers. The MF maximizes the response of known endmembers and suppresses the effect of the background. The higher the resultant MF output for a pixel, the higher the likelihood of the match between the pixel spectrum and the target material is.

RESULTS AND DISCUSSION

SPECTRAL FEATURES OF MINERALS

1. Feldspars

Visible and near Infrared (0.35 μ m to 2.50 μ m) spectral features of feldspars are characterized by diffuse absorption features about 1.1 to 1.3 μ m wavelength region caused by Fe²⁺ iron oxides. If water is incorporated in the structure some water absorptions may be also observed. The wavelength of the absorption increases with increasing Fe²⁺ content. The highest content of Fe²⁺ (up to 0.5wt%) corresponds to deepest absorption bands. The Fe²⁺ iron contents increase with increasing anorthite content up to An₆₅. Except for the diffuse absorption at 1.1 to 1.3 μ m, plagioclase has no spectral features at 2.1 to 2.5 μ m wavelength region. The reflectance is fairly high at the visible spectrum wavelengths. The relative proportion of plagioclase to ferromagnesian minerals can be obtained by a band ratio of $(b_2+b_3)/(b_7+b_8)$ (Adams, Goullud, 1978; Crown, Pieters, 1987).

2. Epidote, chlorite, pyroxenes, olivine

Both ferrous and ferric iron in minerals cause strong absorptions between 0.8 and 2.4 μ m wavelength. Ferric minerals most often exhibit an absorption near 0.9 μ m (Hunt, 1977; Horgan *et. al.*, 2014). The strongest ferrous iron absorption band varies between 0.9 and 1.4 μ m most often centering near 1.0 to 1.1 μ m. Many iron-bearing minerals such as pyroxenes additionally exhibit another absorption band usually centered near 2 μ m, but varying between 1.8 and 2.4 μ m. Orthopyroxene displays a relatively narrow absorption

band near 0.9um, and a broad absorption band centered near 1.9um. High and low-calcium clinopyroxenes behave different to each other. Some clinopyroxenes exhibit a narrow, symmetrical absorption band centered near 1.05um and a broad absorption band near 2.2um. Other types of clinopyroxene may show a complex absorption band near 1.0um and no 2.0um. The 1.0um band is actually a combination of two or three distinct bands centered near 0.94, 1.03, and 1.15um (Horgan *et. al.*, 2014) (Figure 2).

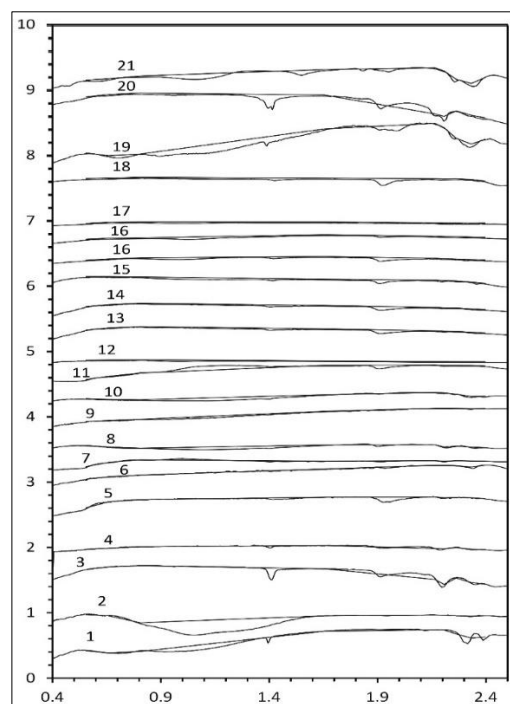


Figure 2. The spectra of minerals and rocks abundant in igneous, and sedimentary environments. 1. Amphibole, 2. Olivine, 3. Illite, 4. Quartzite, 5. Feldspar, 6. Limestone, 7. Sandstone, 8. Illite-bearing Shale, 9. Granodiorite, 10. Diorite, 11. Rhyolite, 12. Basaltic Andesite, 13. Quartz Monzonite, 14. Quartz Monzonite, 15. Nepheline Syenite, 16. weathered Basalt, 17. Pyroxene Basalt, 18. fresh Basalt 19. Nepheline, 20. Chlorite, 21. Kaolinite, 22. Epidote.

Source: Horgan *et. al.*(2021).

Olivine shows a broad and asymmetric absorption band centered near 1.05um, and no 2.0um absorption band. The 1.0um band is a combination of three bands centered near 0.85, 1.05, and 1.15um (Horgan *et. al.*, 2014). Other Fe-bearing minerals, such as iron oxides, iron-bearing clays, and ferric sulfates often exhibit absorption bands near 0.9 to 1.1um (Horgan *et. al.*, 2014). The ferric iron (Fe⁺³) has a strong absorption at around 0.45um

wavelength coinciding with ASTER band 1. Epidote, chlorite, and other ferromagnesian minerals with hydroxyl groups show a strong absorption for F-OH vibrations at around 2.20 to 2.30um wavelength coinciding with ASTER band bands 8 and 7 (Clark *et. al.*, 1990).

3.Quartz

Quartz does not show any diagnostic absorption features in the SWIR spectral region. Therefore, the multispectral thermal infrared (TIR) data of ASTER are vital for detecting non-hydrous varieties of quartz (Rockwell and Hofstra 2008). Si-O absorption features occur near 8.7um wavelength coinciding with ASTER band 11 which enables mapping of acidic volcanic and igneous rock (Rockwell and Hofstra 2008, Rajendran *et. al.* 2011). Despite this, ASTER thermal infrared data have a spatial resolution of 90 meters and thermal bands cannot be used for successful detection of siliceous rocks (Rasouli Beirami and Tangestani 2020). Hydrous varieties of quartz in silicate minerals may show an absorption at ASTER band 4 due to hydroxyl vibrations Rajendran and Nasir 2014.

4. Carbonate minerals

Carbonate rocks predominantly are composed of calcite and dolomite. Dolomite and calcite have distinct spectral features (Hunt *et. al.*, 1972; Hunt, 1977; Beirami, Tangestani, 2020). The calcite absorption band is at 2.35um coinciding with ASTER band 8 and that of dolomite is at 2.33um coinciding with ASTER band 7 (Zaini *et. al.*, 2014). Calcite and dolomite can be distinguished and identified by variations in their absorptions between 2.33 and 2.45um (Rowan, Mars, 2003). Calcite and dolomite also have strong absorption positions in the thermal infrared region at 11.40 and 11.35um, respectively (Rockwell, Hofstra, 2008). (Rajendran *et. al.*, 2011). Dolomite and calcite can be identified by calculating ASTER band ratio $b8/b7$ (Beirami, Tangestani, 2020) (Figure 2).

5. Clay minerals

Al-OH absorption features of clay minerals, including kaolinite and mica occur near 2.10 to 2.20um wavelength. Hydroxyl group also has a doublet absorption at around 1.4um. Illite and muscovite have additional absorption bands at 2.35 to 2.45um. Mg-OH absorptions

occur at a similar wavelength at around 2.30um (Clark *et. al.*, 1990). Therefore, these hydroxyl absorption features can be detected at ASTER band 6 (Figure 2).

6.PCA image

Because vegetation is considered to be a culprit spectral material in PCA transformation (Grebby *et. al.*, 2014), the vegetated and cultivated areas were masked out of the image by applying an NDVI mask image. The false color composite image created by assigning PCA b1,b2,b3 to RGB is shown in figure 3. It can be seen that most of the sedimentary rocks and alluvium are shown in green, whilst many igneous and volcanic rocks are depicted in red.

Many areas covered by dark basalts (Qp) are shown in red. However, there are some exceptions. Some sedimentary units such as the shale denoted by Ksh,t is depicted in red. In contrast, some volcanic and igneous rocks denoted by r01, r02, and r03 are depicted in green. The PCA results show that the spectral differences between various rock units in the area are very subtle. Otherwise, stark differences between different lithologic units would be visible on the PCA image. The PCA image is usually used to reveal such differences (Rajendran *et. al.*, 2011).

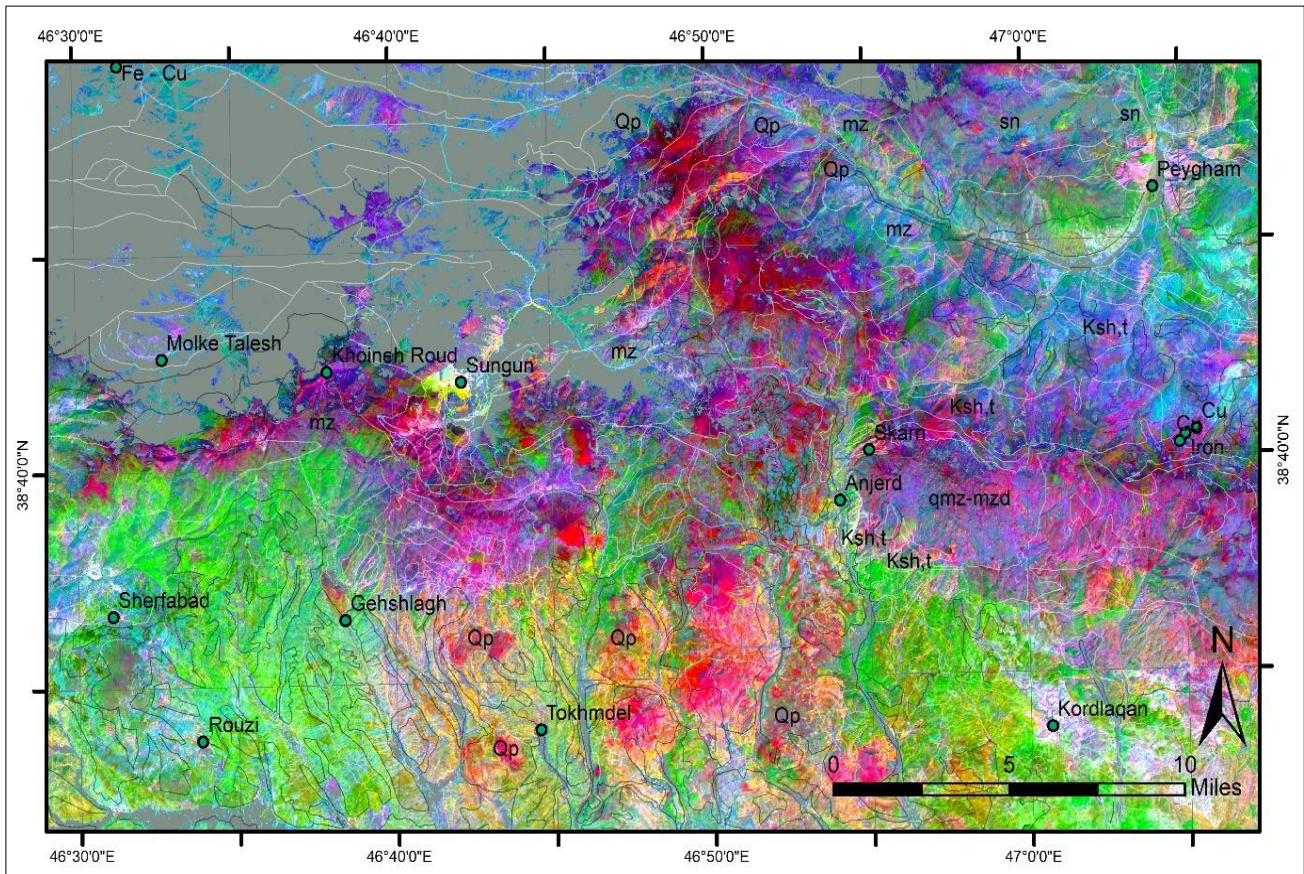


Figure 3. The false color composite created from the PCA image by assigning PC1PC2PC3 to RGB. Dark basalts and pyroxene basalts mostly appear red due to high values of PC1. Monzonites (mz) and Shiur Daghy quartz monzonite (qmz-mzd) appear red or reddish blue. Most of the sedimentary rocks and alluvium appear green, but some shale and sedimentary rocks (Ksh,t) appear blue or reddish blue. Vegetation is shown in black.

Source: Authors (2021).

FALSE COLOR COMPOSITES AND ASTER RATIO IMAGES

Several band ratios of ASTER imagery in the form of false color composites (FCC) are suggested for mapping meta-sediments and volcanoclastics. A color composite consisting of b_5/b_3 , and b_1/b_2 band ratio express the spectral slope caused by combined effect of ferrous-iron absorption in the VNIR part of the spectrum and the general lack of Al-OH absorption feature in band 5. A false color composite consisting of b_4/b_7 , b_3/b_4 , b_2/b_1 as RGB is used for separating igneous rocks from sedimentary rocks (Abdeen *et. al.*, 2001). Band ratios b_7/b_6 , b_6/b_5 , b_6/b_4 as RGB are used for mapping gneiss domes and granites (Wolters *et. al.*,

2005) and band ratios $b8/b5$, $b5/b4$, $b7/b8$ as RGB are used for distinguishing alkali granites (Madani, Emam, 2009).

Vegetation is a huge setback for lithologic mapping by satellite imagery. Vegetation can obscure the underlying spectral features of the rock substrate and inhibit detection of rock lithologies. This is more acute and troublesome in some igneous terrains composed of rocks of low albedo (Grebby *et. al.*, 2014). Vegetation can have various spectral features during various stages of senescence and livelihood (Baldrige *et. al.* 2009). Therefore, green and dry vegetation can behave differently and mimic the spectral features of rock and mineral spectral materials of interest (Grebby *et. al.*, 2014; Beirami, Tangestani, 2020). Therefore, it is most often desirable to mask vegetation out of image by utilizing the normalized difference vegetation index (NDVI) defined as $(b3-b2)/(b3+b2)$ (Bertoldi *et. al.*, 2011; Meer *et. al.*, 2014). In the northwestern part of the study area, vegetation cover is quite thick and therefore a minimum threshold on an NDVI image was used to mask out the vegetation.

The shape of the rock spectra in the VNIR part of the spectrum are often affected by ferric-iron and ferrous-iron absorption intensities (Rowan *et. al.*, 2005). Ferric-iron absorptions cause a decrease in reflectance in band 1. Ferrous iron does not have the same strong absorptions in band 1 and therefore show higher $b1/b2$ ratios.

$(b7 + b9) / (b8 + b8)$ band ratio is sensitive to Fe-OH and Mg-OH absorptions in observed in epidote and chlorite and other ferromagnesian minerals in the study area (Dalton *et. al.*, 2004; Beirami, Tangestani, 2020). Therefore, it is very well known that Fe-OH, Mg-OH and CO₃ absorption features are not distinguishable from each other solely based on relative band depth calculations (Rowan, Mars, 2003; Dalton *et. al.*, 2004). In order to distinguish carbonate rocks from igneous rocks, it is required to consider albedo as well. Carbonate rocks generally show higher albedo relative to volcanic, and other types of igneous rocks (Beirami, Tangestani, 2020).

Figure 4 shows a false color composite image created from band ratios b_4/b_7 , b_3/b_4 , b_2/b_1 as RGB. Vegetation was assigned zero digital numbers so that the variation in coloring of rock units of interest could be better revealed. As the image shows the volcanic and igneous rocks appear red, pink or blue. In contrast, sedimentary terrains mostly appear green in the image. The FCC image resembles the PCA image. This shows that the PCA image reflected the variation in spectral features in this false color composite. The volcanic and igneous rocks in the image have high $4/7$ and $2/1$ ratios, and low b_3/b_4 ratios in contrast to the sedimentary terrains which mostly have high b_3/b_4 ratios. Therefore, the volcanic and igneous rocks could be discriminated from sedimentary rocks by thresholding b_3/b_4 band ratio. The resulting output of b_3/b_4 thresholding is shown in figure 5 after overlaying the results on the geologic map previously shown in figure 5. As the image shows the threshold has been able to discriminate sedimentary rocks from igneous rocks in most of the areas except for area denoted r01, r02, and r03. In the aforementioned areas the threshold shows that the rocks must be of sedimentary origin, but the lithologic map shows they are volcanic rocks. Additionally, most of the tuff and volcanoclastic rocks are classified into igneous and volcanic rocks. In region r04 and r05 the threshold shows that the rocks are of volcanic and igneous origin, but the lithologic map shows they are of sedimentary origin.

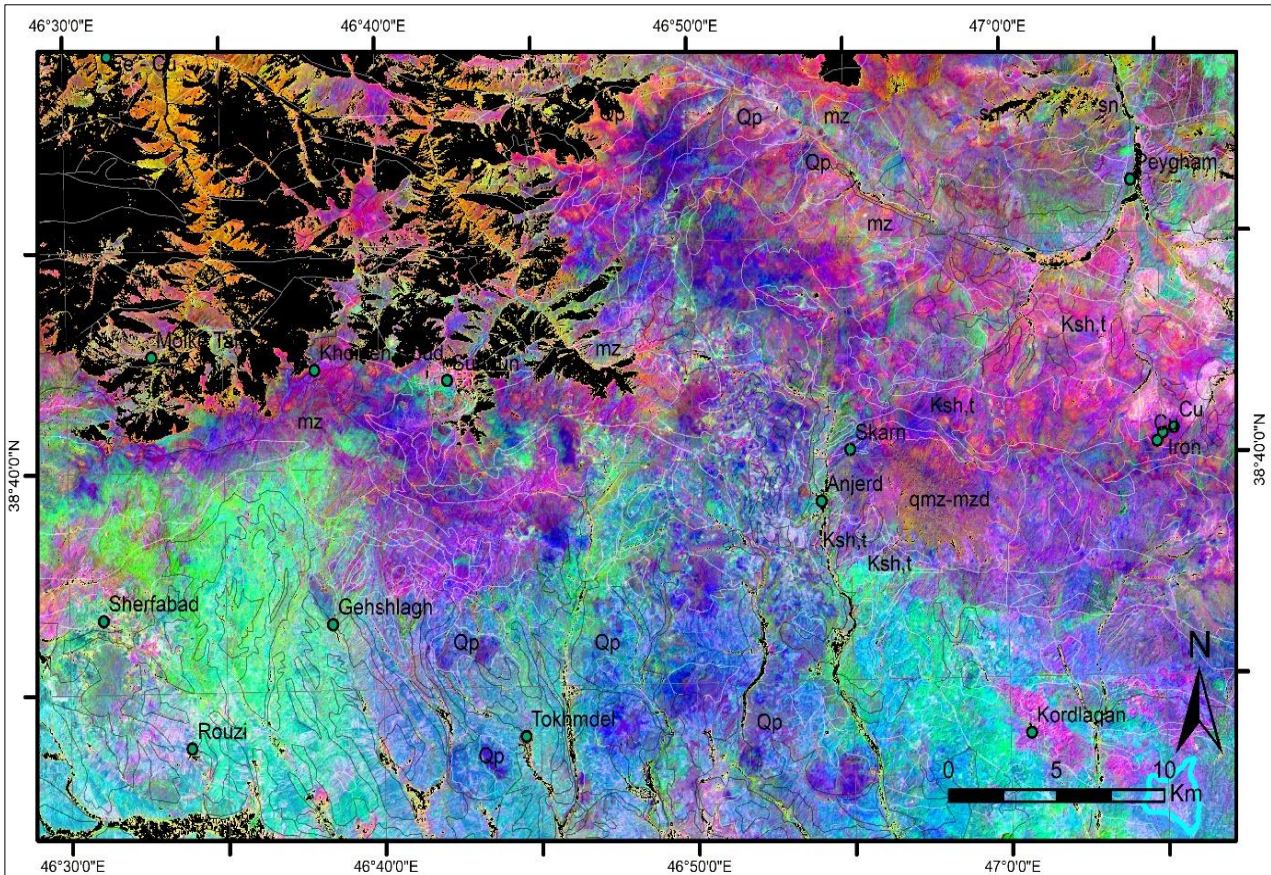


Figure 4. The b4/b7, b3/b4, b2/b1 false color composite (FCC). Most of the sedimentary rocks appear light green except for shale (Ksh,t) and limestone which appear blue or reddish blue. Quartz monzonite (qmz-mzd) and monzonite (mz) and other intrusive rocks and volcanic rocks appear blue, reddish blue or red. Vegetation is shown in black.

Source: Authors (2021).

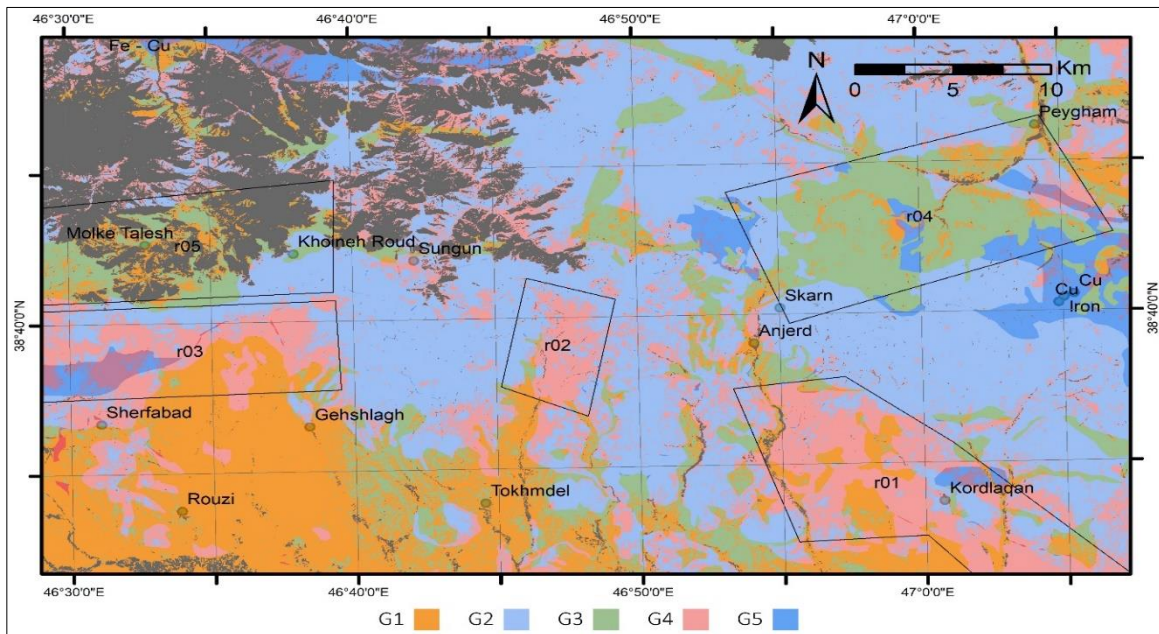


Figure 5. The b3/b4 band ratio image. G1 denotes the sedimentary rocks which have high b3/b4 band ratios, G2 are the volcanic and igneous rocks with low b3/b4 band ratios, G3 denotes the sedimentary rocks with low b3/b4 band ratios, and G4 denotes the igneous or volcanic rocks which have high b3/b4 band ratios, and G5 denotes tuff and volcanoclastic rocks which mostly have low b3/b4 band ratios. In r01, r02, and r03 regions the volcanic rocks show high b3/b4 band ratios, in contrast to region r04 and r05 in which sedimentary rocks have low b3/b4 band ratios. Vegetation is shown in black.

Source: Authors (2021).

Propylitic alteration is the transformation of ferromagnesian minerals into quartz, chlorite, epidote, calcite, dolomite, and albite (Sinclair, 2007). In contrast, phyllic alteration zones consist of quartz, sericite, and pyrite. Additionally, argillic alteration consists of a combination of quartz, illite, pyrite, kaolinite, smectite, montmorillonite, and calcite (Sinclair, 2007). Except for quartz which is infrared inactive in SWIR spectral range, other minerals of propylitic alteration show an absorption in ASTER band 8 and to some extent in band 7 (Dalton *et. al.*, 2004, Beirami, Tangestani, 2020). Therefore, propylitic alteration can be detected by using ASTER propylitic alteration mineral index $(b6 \times b9) / (b8 \times b8)$. Ferromagnesian minerals generally have absorptions in bands 7 and 8 (Singer, 1981; Crown, Pieters, 1987; Horgan *et. al.*, 2014) due to presence of iron and magnesium oxides (Rowan, Mars, 2003). Therefore, the aforementioned index can also detect ferromagnesian minerals. However, when mafic rocks are not present the aforementioned mineral index delineates

the areas of propylitic alteration. The propylitic alteration zones identified by the mentioned method are depicted in figure 6. It can be observed that propylitic alteration zone has affected some parts of Sheyvar Daghi monzonite body.

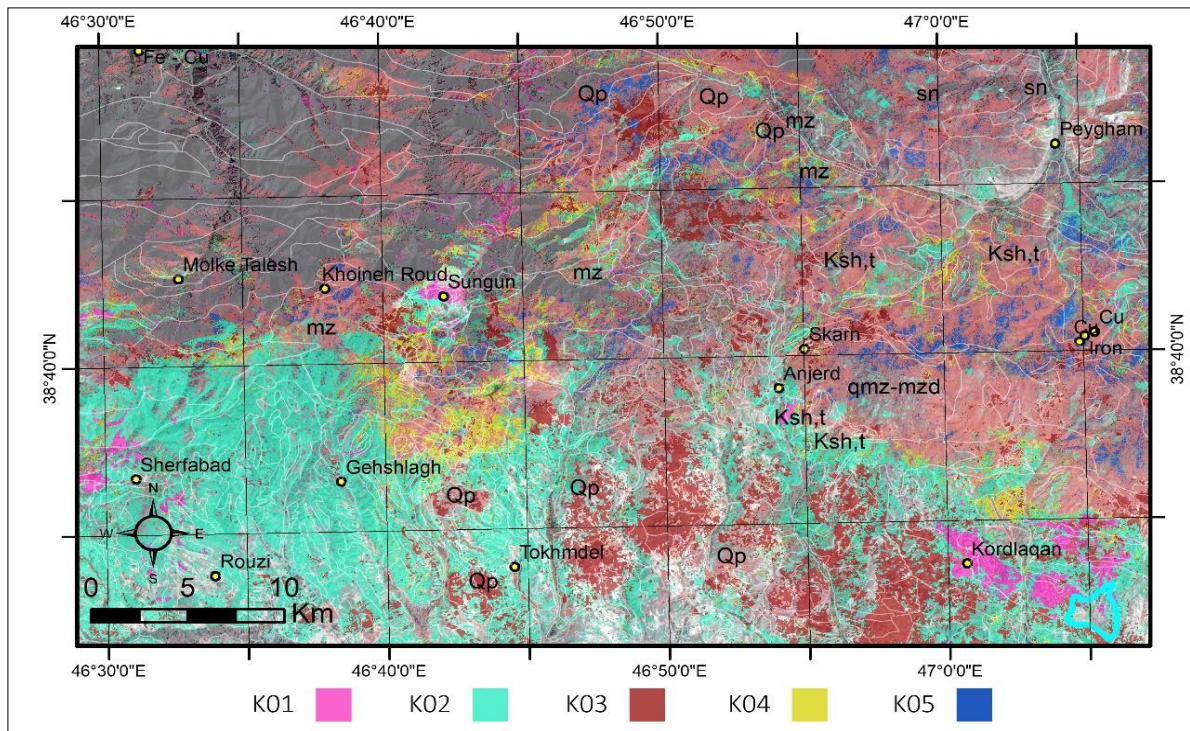


Figure 6. The lithological map of the study area produced by a combination of MF, SAM and band ratio calculations. The K01 denotes highly altered volcanic rocks, K02 denotes sedimentary rocks identified by MF, and K03 denotes dark basalts with higher content of ferromagnesian minerals including pyroxene. K04 and K05 show zones of argillic alteration, and propylitic alteration, respectively.

Source: Authors (2021).

Illite, kaolinite, sericite, and various clay minerals most abundant in phyllic and argillic mineralization have an absorption coinciding with ASTER band 6. Hence, the presence of these minerals can be detected by Bierwith’s clay mineral index defined as $(b5 \times b7)/(b6 \times b6)$ (Bierwith, 2002; Kalinowski, Oliver, 2004; Testa *et. al.*, 2018) or similarly by using $(b5+b7)/b6$ band ratio image (Rowan and Mars 2003), or by $(b4 + b7) / (b6 + b6)$ (Rowan *et. al.*, 2005). These band ratios can also be used for detection of soil, and clay in alluvial deposits (Beirami, Tangestani, 2020). However, where rocks are of igneous or volcanic type, the index can be used to delineate argillic and phyllic alteration zones. The argillic alteration distribution zones produced by the aforementioned method shows that argillic alteration

zones are more prevalent at granodiorite, monzonite, dacite, trachyte, and ignimbrite rocks around Sungun copper deposit and at the vicinity of the deposit up to about 8 kilometers to the south and west of the deposit. This is conformant with the association of copper deposits with intense alteration halos (Hezarkhani, 2006). Sheyvar Daghy quartz-monzonite intrusive body does not show any signs of argillic alteration except for at the vicinity of skarn rock unit at the northern part of the intrusion.

7.SAM images

The spectra of various igneous rock units shown in figure 7 were fed into SAM algorithm to test the capability of this algorithm in mapping the rocks. The SAM algorithm was able to differentiate igneous and volcanic rocks from sedimentary rocks and alluvium deposits. The result of SAM algorithm in separating sedimentary rocks from igneous and volcanic rocks was very similar to that of PCA image shown in figure 3 and b3/b4 band ratio image shown in figure 4. Although SAM algorithm is sensitive enough to the spectral difference between magmatic rocks and sedimentary rocks, the results showed that it is not sensitive to spectral variations of more similar lithologic units. Additionally, SAM resultant images have low standard deviations of image pixel digital numbers and therefore the distinction between the target and background materials is not unambiguous. Therefore, the SAM algorithm was not chosen for further image processing.

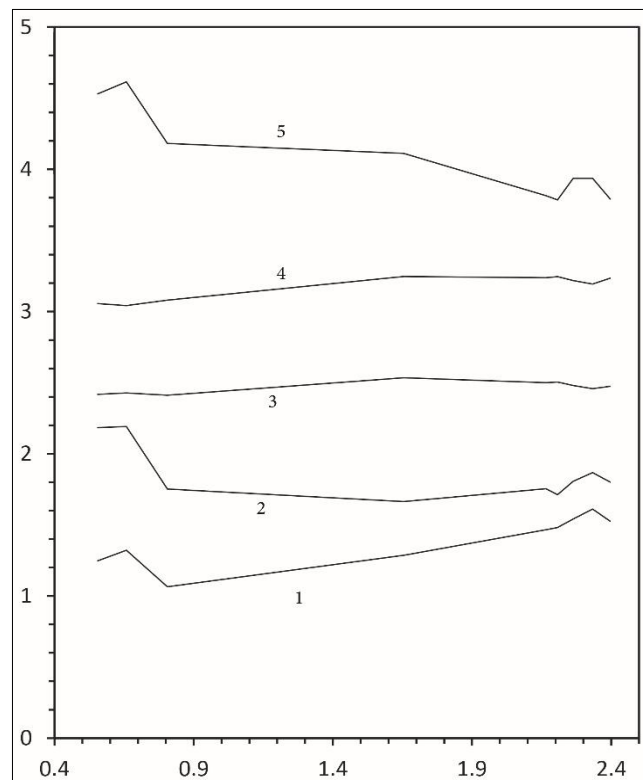


Figure 7. The spectra extracted from the IAR image. 1: dark igneous/volcanic rocks with higher pyroxene contents, 2, and 3: sediments, 4: igneous/volcanic rocks, 5: highly altered rocks with ferric iron absorptions.

Source: Horgan *et. al.*(2021).

8. Matched Filtering (MF) images

The spectra shown in figure 7 were fed into matched filtering (MF) algorithm to test the efficacy of this algorithm. The results are shown in Figure 6. The spectra chosen as an input to the algorithm are those shown in figure 7. As it was shown in figure 2, the spectral distinction between igneous and volcanic rocks is very subtle and their difference cannot be detected by ASTER imagery. The results show that akin to SAM algorithm, MF algorithm also cannot distinguish between volcanic and igneous rocks.

Examination of true color composite images of Landsat 8 imagery shows that at the southern part of the study area, there is a patch of altered ignimbrite and highly altered volcanic rocks with show absorption characteristics of ferric iron oxides. These rocks show low pixel values in PCA band 5. The spectra of these rocks are shown in figure 7. In order to detect these rocks, the average spectra of the rock unit were fed into MF algorithm. As the result is figure 6 shows, the MF algorithm was able to distinguish these highly altered rocks.

It can be seen that most of the rocks at the Songun copper deposit are also highly altered and show characteristic absorption features of ferric ion oxides. This is because continued mining activity in the deposit has led to intense weathering and dissolution of sulfur minerals and release of iron from copper-iron sulfides such as pyrite. The highly altered rocks are denoted by K01 in figure 6 and are shown in rectangular area of r07 and r08.

As shown in figure 6, the MF can also distinguish dark basalt and igneous rocks with higher content of pyroxene and/or olivine minerals (denoted by K03) from other magmatic rocks.

Shale and clay minerals have an absorption feature in ASTER band 6. To detect the sedimentary rocks with abundant clay such as shale, the spectrum of argillaceous sedimentary rocks extracted from IARR image as shown in figure 7, fed into MF algorithm. The results show that most of the sedimentary clastic rocks in the area are mixed with volcanoclastic detrital material and the extent of pure sedimentary rocks is very limited. In fact, rigorous examination of the geologic maps of the area shows that sedimentary rocks in the study area have significant contents of volcanoclastic material. Specially in the southern part of the study area the terrain shows low elevation and most of the volcanic rocks have made their way into alluvial fans. Therefore, in these areas, the sedimentary and volcanic rocks are intricately mixed and they cannot be distinguished by MF algorithm.

In order to distinguish areas of intense argillic alteration, areas of higher concentration of argillic material were distinguished by applying $(b5 \times b7) / (b6 \times b6)$ band ratio, and then the resultant image was masked by volcanic and magmatic rocks to detect argillic alteration. Similarly, to detect propylitic alteration, $(b6 \times b9) / (b8 \times b8)$ band ratio was masked by magmatic and volcanic rocks. The results are shown in figure 6. Comparison of the classified image in figure 6 with ground truth image reproduced from the geological maps of the area shows that the overall accuracy of the classification is no less than 0.79, and that the Kappa coefficient for each class does not fall below 0.67. The values just mentioned are

considered very good for lithologic classification images produced from ASTER satellite imagery.

CONCLUSION

By analyzing satellite imagery, it was shown that the spectral features of the igneous and volcanic rocks in the study area are fairly the same. This is due to quartz and feldspar being fairly featureless in SWIR spectral range. However, it was shown that a combination of PCA, MF, and band ratioing can be used to separate igneous and volcanic rocks from sedimentary rocks and delineate the zones of argillic and propylitic alteration. As it was shown the most intense argillic alteration along with moderate propylitic alteration occurs around Sungun porphyry copper deposit. Argillic alteration is non-existent at Sheyvar Daghi monzonite body, except for at the vicinity of skarn deposit. In contrast, propylitic alteration occurs moderately at Sheyvar Daghi monzonite body. It is concluded that the applicability of ASTER imagery to mapping igneous and volcanic terrains is limited, but mapping such a terrain with right methods can reveal useful information in such regions and most probably reveal the locations of porphyry copper mineralization.

REFERENCES

- ABDEEN, M. M.; ALLISON, T. K.; ABDELSALAM, M. G.; STERN, R. J. Application of ASTER band-ratio images for geological mapping in arid regions; the neoproterozoic Allaqi Suture, Egypt. *In Annual meeting of Geological Society of America, United States of America*, November 5-8, 2001 (Vol. 3, pp. 289, Vol. 3): Geological Society of America.
- ADAMS, J. B.; GOULLUD, L. H. **Plagioclase feldspars: Visible and near infrared diffuse reflectance spectra as applied to remote sensing**. Paper presented at the Proceedings of the Lunar and Planetary Science Conference, 1978.
- AGARD, P.; OMRANI, J.; JOLIVET, L.; WHITECHURCH, H.; VRIELYNCK, B.; SPAKMAN, W. Zagros orogeny: a subduction-dominated process. *Geological Magazine: Geodynamic evolution of the Zagros*, 148(5-6), 2011. p. 692-725. doi: 10.1017/S001675681100046X.
- ALAVI, M. Structures of the Zagros fold-thrust belt in Iran. *American Journal of Science*, 307(9), p. 1064-1095, 2007. doi:10.2475/09.2007.02.
- ASADZADEH, S.; SOUZA FILHO, C. R. A review on spectral processing methods for geological remote sensing. *International Journal of Applied Earth Observation and Geoinformation*, 47, 2016. P. 69-90, doi:10.1016/j.jag.2015.12.004.

- ASHRAFI, N.; HASEBE, N.; JAHANGIRI, A. Cooling history and exhumation of the Nepheline Syenites, NW Iran: Constraints from Apatite fission track. **Iranian Journal of Earth Sciences**, 10(2) 2018. p. 109-120.
- BABAKHANI, A. R.; LESQUYER, J. L.; RICO, R. **Geological Map of Ahar Quadrangle** (Scale 1:250,000). Tehran: Geological Survey of Iran, 1990.
- BALDRIDGE, A. M.; HOOK, S. J.; GROVE, C. J.; RIVERA, G. The Aster Spectral Library version 2.0. **Remote Sensing of Environment**, 113, 2009. p. 711–715.
- BARATIAN, M.; ARIAN, M.A.; YAZDI, A. (2020) Petrology and Petrogenesis of Siah Kooch volcanic rocks in the eastern Alborz, *GeoSaber*, v. 11, 2020. p. 349-363. DOI: <https://doi.org/10.26895/geosaber.v11i0.980>
- BAZIN, D.; HÜBNER, H. Copper Deposits in Iran. **International Report** (Vol. 13, pp. 87-93). Tehran: Geological Survey of Iran, 1969.
- BEN-DOR, E.; KRUSE, F. A. The relationship between the size of spatial subsets of GER 63 channel scanner data and the quality of the Internal Average Relative Reflectance (IARR) correction technique. **International Journal of Remote Sensing**, 15, 1994. p. 683-690, doi:10.1080/01431169408954107.
- BERNSTEIN, L. S.; JIN, X.; GREGOR, B.; GOLDEN, S. M. A. Quick atmospheric correction code: algorithm description and recent upgrades. **Optical Engineering**, 51, 11, 2012. doi:10.1117/1.OE.51.11.111719.
- BERTOLDI, L.; MASSIRONI, M.; VISONÀ, D.; CAROSI, R.; MONTOMOLI, C.; GUBERT, F. Mapping the Buraburi granite in the Himalaya of Western Nepal: Remote sensing analysis in a collisional belt with vegetation cover and extreme variation of topography. **Remote Sensing of Environment**, 115, 2011, p. 1129-1144. doi:10.1016/j.rse.2010.12.016.
- BIERWITH, P. **Evaluation of ASTER Satellite Data for Geological Applications**. Consultancy Report to Geoscience Australia. Canada, 2002.
- BOARDMAN, J. W.; KRUSE, F. A.; GREEN, R. O. Mapping target signatures via partial unmixing of AVIRIS data. **Fifth JPL Airborne Earth Science Workshop Summaries**, v. 95-1, 1995. p. 23-26.
- CLARK, R. N.; KING, T. V. V.; KLEJWA, M. K.; SWAYZE, G. A.; VERGO, N. High Spectral Resolution Reflectance Spectroscopy of Minerals. **Journal of Geophysical Research**, 95, 1990. p. 12653-12680. doi:10.1029/JB095iB08p12653.
- CROSTA, A. P.; MCMOORE, J. Enhancement of landsat Thematic Mapper imagery for residual soil mapping in SW Minas Gerais State Brazil: a prospecting case history in greenstone belt terrain. **Paper presented at the Seventh Thematic Conference on RemoteSensing for Exploration Geology**, ERIM, Calgary, Alberta, Canada, 1989.
- CROWLEY, J. K. Mapping playa evaporite minerals with AVIRIS data: A first report from Death valley, California. **Remote Sensing of Environment**, 44, 1993. p. 337-356. doi:10.1016/0034-4257(93)90025-S.

CROWLEY, J. K.; BRICKEY, D. W.; ROWAN, L. C. Airborne imaging spectrometer data of the Ruby Mountains, Montana: mineral discrimination using relative absorption band-depth images. **Remote Sensing of Environment**, 29, 1989. p. 121– 134.

CROWN, D. A.; PIETERS, C. M. Spectral properties of plagioclase and pyroxene mixtures and the interpretation of lunar soil spectra. **Icarus**, 27(3), 1987. p. 492-506. doi:10.1016/0019-1035(87)90047-9.

DALTON, J. B.; BOVE, D. J.; MLADINICH, C. S.; ROCKWELL, B. W. Identification of spectrally similar materials using the USGS Tetracorder algorithm: The calcite-epidote-chlorite problem. **Remote Sensing of Environment**, 89, 2004. p. 455-466, doi:10.1016/j.rse.2003.11.011.

GAO, B. C.; MONTES, M. J.; DAVIS, C. O.; GOETZ, A. F. H. Atmospheric correction algorithms for hyperspectral remote sensing data of land and ocean. **Remote Sensing of Environment**, 113, 2009. p. 17-24. doi:10.1016/j.rse.2007.12.015.

GHADIMI, F.; KHAVARI, M. Comparison of original and weighted singularity index in separation of Pb-Zn mineralized zone in the Haft Savaran district, Central Iran. **Iranian Journal of Earth Sciences**, 11(2) 2019. p. 160-170.

GREBBY, S.; CUNNINGHAM, D.; TANSEY, K.; NADEN, J. The impact of vegetation on lithological mapping using airborne multispectral data: A case study for the north Troodos region, Cyprus. **Remote Sensing**, 6, 2014. p. 10860-10887, doi:10.3390/rs61110860.

HEZARKHANI, A. Geochemistry of the Enjerd Skarn and Its Association with Copper Mineralization, Northwestern Iran. **International Geology Review**, 48, 2007. p. 892–909, doi:10.2747/0020-6814.48.10.892.

HEZARKHANI, A. Petrology of the intrusive rocks within the Sungun Porphyry Copper Deposit, Azerbaijan, Iran. **Journal of Asian Earth Sciences**, 27, 2006. p. 326-340.

HORGAN, B. H. N.; CLOUTIS, E. A.; MANN, P.; BELL III, J. F. Near-infrared spectra of ferrous mineral mixtures and methods for their identification in planetary surface spectra. **Icarus**, 234, 2014. p. 132-154, doi:10.1016/j.icarus.2014.02.031.

HUNT, G. R. Spectral signatures of particulate minerals in the visible and near infrared. **Geophysics**, 42(3), 1977. p. 501– 513.

HUNT, G. R.; SALISBURY, J. W.; LENHOFF, C. R. Visible and nearinfrared spectra of minerals and rocks: V. Halides, phosphates, arsenates, vanadates, and borates. **Modern Geology**, 3, 1972. p. 121– 132.

JAMSHIDIBADR, M.; TARABI, S.; GHOLIZADEH, K. Study of micro-textures and chemistry of feldspar minerals of East Sarbisheh volcanic complex (Eastern Iran), for evidence of magma chamber process. **Iranian Journal of Earth Sciences**, 12(1) 2020. p. 10-31.

KALINOWSKI, A.; OLIVER, S. ASTER Mineral Index Processing Manual. (pp. 36). Australia: **Geoscience Australia**, 2004.

KRUSE, F. A. Use of airborne imaging spectrometer data to map minerals associated with hydrothermally altered rocks in the northern grapevine mountains, Nevada, and California. **Remote Sensing of Environment**, v. 24, 1988. p. 31-51.

KRUSE, F. A.; LEFKOFF, A. B.; BOARDMAN, J. B.; HEIDEBRECHT, K. B.; SHAPIRO, A. T.; BARLOON, P. J. The Spectral Image Processing System (SIPS) – Interactive Visualization and Analysis of Imaging Spectrometer Data. **Remote Sensing of Environment**, 44, 1993. p. 145–163.

MADANI, A.; EMAM, A. A. SWIR ASTER band ratios for lithological mapping and mineral exploration: A case study from El Hudi area, southeastern desert, Egypt. **Arabian Journal of Geosciences**, 4, 2009. p.45–52.

MEER, F. D.; DERWERFF, H. M. A. V.; RUITENBEEK, F. J. A. V. Potential of ESA's Sentinel-2 for geological applications. **Remote Sensing of Environment**, 148, 2014. p. 124-133, doi:10.1016/j.rse.2014.03.022.

MOLLAI, H. **Petrochemistry and genesis of the granodiorite and associated iron-cooper skarn deposit of Mazraeh**, Ahar, East-Azarbayjan, Iran, 1991.

MOLLAI, H.; DAVE, V. K. S.; SHARMA, R. Copper mineralization at Mazraeh NorthWest of Iran: Evidences for fluid evolution and Skarn deposit. **Ore Geology Reviews**, 2009

MOLLAI, H.; SHARMA, R.; PE-PIPER, G. Copper mineralization around the Ahar batholith, north of Ahar (NW Iran): Evidence for fluid evolution and the origin of the skarn ore deposit. **Ore Geology Reviews**, 35(3-4), 2009a. p. 401-414, doi:10.1016/j.oregeorev.2009.02.005.

NAZEMI, E.; ARIAN, M. A.; JAFARIAN, A.; POURKERMANI, M.; YAZDI, A. Studying The Genesis Of Igneous Rocks In Zarin-Kamar Region (Shahrood, Northeastern Iran) By Rare Earth Elements, **Revista Gênero e Direito**, 8(4), 2019. p. 446-466. DOI: <https://doi.org/10.22478/ufpb.2179-7137.2019v8n4.48442>

RAJENDRAN, S.; HERSI, O. S.; AL-HARTHY, A.; AL-WARDI, M.; EL-GHALI, M. A.; AL-ABRI, A. H. (). Capability of advanced spaceborne thermal emission and reflection radiometer (ASTER) on discrimination of carbonates and associated rocks and mineral identification of eastern mountain region (Saih Hatat window) of Sultanate of Oman. **Carbonates and Evaporites**, 26, 2011. p. 351-364, doi:10.1007/s13146-011-0071-4.

RAJENDRAN, S.; NASIR, S. ASTER spectral sensitivity of carbonate rocks - Study in Sultanate of Oman. **Advances in Space Research**, 53, 2014. p. 656-673, doi:10.1016/j.asr.2013.11.047.

RAJENDRAN, S.; NASIR, S.; KUSKY, T. M.; GHULAM, A.; GABR, S.; EL-GHALI, M. A. K. Detection of hydrothermal mineralized zones associated with listwaenites in Central Oman using ASTER data. **Ore Geology Reviews**, 53, 2013. p. 470–488, doi:10.1016/j.oregeorev.2013.02.008.

RASOULI BEIRAMI, M., & TANGESTANI, M. H. A New Band Ratio Approach for Discriminating Calcite and Dolomite by ASTER Imagery in Arid and Semiarid Regions. **Natural Resources Research**, 2020. doi:10.1007/s11053-020-09648-w.

RICHTER, R.; SCHLÄPFER, D. **Atmospheric / Topographic Correction for Satellite Imagery: ATCOR-2/3 User Guide, Version 8.2 BETA**. (8.2 BETA ed., pp. 203). Switzerland: ReSe, 2012.

ROCKWELL, B. W.; HOFSTRA, A. H. Identification of quartz and carbonate minerals across northern Nevada using ASTER thermal infrared emissivity data—Implications for geologic mapping and mineral resource investigations in well-studied and frontier areas. **Geosphere**, 4, 218, 2008. doi:10.1130/GES00126.1.

ROWAN, L. C.; MARS, J. C. Lithologic mapping in the Mountain Pass, California area using Advanced Spaceborne Thermal Emission and Reflection Radiometer (ASTER) data. **Remote Sensing of Environment**, 84, 2003. p. 350-366. doi:10.1016/S0034-4257(02)00127-X.

ROWAN, L. C.; MARS, J. C.; SIMPSON, C. J. Lithologic mapping of the Mordor, NT, Australia ultramafic complex by using the Advanced Spaceborne Thermal Emission and Reflection Radiometer (ASTER). **Remote Sensing of Environment**, 99(1), 2005. p. 74–87, doi: 10.1016/j.rse.2004.11.021.

RSI ENVI user's guide, the environment for visualizing images, version 4.1. Boulder, Colorado: Research Systems Incorporated, 2004

SINCLAIR, W. D. Porphyry deposits. In M. D. Division (Ed.), **Mineral Deposits of Canada: A Synthesis of Major Deposit-Types, District Metallogeny, the Evolution of Geological Provinces, and Exploration Methods**, Canada: Geological Association of Canada, 2007. p. 223-243.

SINGER, R. B. Near - infrared spectral reflectance of mineral mixtures: Systematic combinations of pyroxenes, olivine, and iron oxides. **Journal of Geophysical Research**, 1981. p. 7967-7982, doi:10.1029/JB086iB09p07967.

TANGESTANI, M. H.; MAZHARI, N.; AGAR, B.; MOORE, F. Evaluating Advanced Spaceborne Thermal Emission and Reflection Radiometer (ASTER) data for alteration zone enhancement in a semi - arid area, northern Shahr - e - Babak, SE Iran. **International Journal of Remote Sensing**, 29, 2008. p. 2833-2850, doi:10.1080/01431160701422239.

TARABI, S.; EMAMI, M. H.; MODABBERI, S.; SHEIKH ZAKARIAEE, S.J. Eocene-Oligocene volcanic units of Momenabad, east of Iran: petrogenesis and magmatic evolution. **Iranian Journal of Earth Sciences**, 11(2) 2019. p. 126-140.

TESTA, F. J.; VILLANUEVA, C.; COOKE, D. R.; ZHANG, L. Lithological and Hydrothermal Alteration Mapping of Epithermal, Porphyry and Tourmaline Breccia Districts in the Argentine Andes Using ASTER Imagery. **Remote Sensing**, 10(2), 203, 2018. doi:10.3390/rs10020203.

WOLTERS, J. M.; GOLDIN, L.; WATTS, D. R.; HARRIS, N. B. W. Remote sensing of gneiss and granite in southern Tibet. In: **Annual meeting of Geological Society of America**, United States of America, November 5-8, 2001 (Vol. 37, pp. 93): Geological Society of America, 2005.

YAMAGUCHI, Y.; NAITO, C. Spectral indices for lithologic discrimination and mapping by using the ASTER SWIR bands. **International Journal of Remote Sensing**, 24(22), 2003. p. 4311–4323, doi:10.1080/01431160110070320.

YASREBI, A.B.; HEZARKHANI, A. Resources classification using fractal modelling in Eastern Kahang Cu-Mo porphyry deposit, Central Iran. **Iranian Journal of Earth Sciences**, 11(1) pp 2019. p. 56-67.

YAZDI, A.; ASHJA-ARDALAN, A.; EMAMI, M. H.; DABIRI, R.; FOUDAZI, M. Magmatic interactions as recorded in plagioclase phenocrysts of quaternary volcanics in SE Bam (SE Iran). **Iranian Journal of Earth Sciences**, 11(3): 2019. p. 215-224.

YAZDI, A.; ASHJA-ARDALAN, A.; EMAMI, M.H.; DABIRI, R.; FOUDAZI, M. Chemistry of Minerals and Geothermobarometry of Volcanic Rocks in the Region Located in Southeast of Bam, Kerman Province. **Open Journal of Geology**. 7 (11), 2017. P. 1644-1653, doi: 10.4236/ojg.2017.711110

YAZDI, A.; SHAHHOSINI, E.; DABIRI, R.; ABEDZADEH, H. Magmatic Differentiation Evidences And Source Characteristics Using Mineral Chemistry In The Torud Intrusion (Northern Iran). **Revista GeoAraguaia**, 9(2): 2019. p. 6-21.

ZAINI, N.; VAN DER MEER, F.; VAN DER WERFF, H. Determination of Carbonate Rock Chemistry Using Laboratory-Based Hyperspectral Imagery. **Remote Sensing**, 6(5), 2014. p. 4149-4172, doi:10.3390/rs6054149.

ZAINI, N.; VAN DER MEER, F.; VAN DER WERFF, H. Effect of grain size and mineral mixing on carbonate absorption features in the SWIR and TIR wavelength regions. **Remote Sensing**, 4, 2012. p. 987-1003. doi:10.3390/rs4040987.